

Retrieval of elevation by radarclinometry in arid or semi-arid regions

S. LE HÉGARAT-MASCLE, M. ZRIBI and L. RIBOUS

CETP, 10-12 avenue de l'Europe, 78140 Vélizy, France; e-mail: sylvie.mascle@cetp.ipsl.fr

(Received 7 May 2004; in final form 17 February 2005)

The aim of this work is to extend radarclinometry technique to regions where the two current assumptions, (i) Lambertian backscattering and (ii) homogeneous areas, are not possible. For this, we replace the traditional Lambertian model by a backscattering diagram provided by the integral equation model (IEM). Then, to take into account the roughness heterogeneity of the region, we introduce a classification process. In the global algorithm for DEM (digital elevation model), the first iteration classification is determined according to minimum distance, and then the derived altitude is also used to constrain classification. The process is iterative. Validation is performed on four sites in Israel and Tunisia, which represent different cases of arid or semi-arid regions. Both qualitative and quantitative results are satisfactory. Limits of the method are stressed by the sand dune case.

1. Introduction

Since relief is an important parameter of the synthetic aperture radar (SAR) signal observed value, several techniques have been defined to retrieve it from radar measurements. Even if there were great improvements in the knowledge of the Earth's relief through the construction of digital elevation models (DEM), there are still parts of the Earth where point density or DEM accuracy is not sufficient, explaining why this field remains an active domain of investigation. Using radar data and in particular SAR images for DEM estimation, different techniques have been developed (e.g. see the review by Toutin and Gray 2000). We briefly review these techniques.

Interferometry (Gabriel and Goldstein 1988, Massonnet and Rabaute 1993, Small 1998, Petit 2004) needs two SAR phase images corresponding to two different view angles (baseline typically less than a few hundred metres). Any modification of the surface parameters (moisture, roughness, etc.) occurring between the times of the two acquisitions introduces noise in the interferograms. Therefore the temporal coherence between the two acquisitions is a strong constraint. Various propagation effects related to the atmospheric component can also corrupt the differential phase and cause damage to the DEM retrieval. Radargrammetry is very similar to photogrammetry and also needs the acquisition of a stereo pair if possible with opposite-side stereo (Leberl 1979, Toutin 1996). Results are not as good as using visible-infrared data, mainly because of the difficulty in taking into account the specificity of the SAR and surface interaction: DEM accuracy is strongly dependent on the type of relief (Toutin 2000). However, recent works (Simonetto 2002) have shown the opportunity for high resolution radargrammetry.

Radarpolarimetry (Schuler *et al.* 1996, 1998, Lee *et al.* 2002) uses polarimetric SAR data, and, to lead to interesting results, it needs rather strong hypotheses about

surface features and specific polarimetric signatures exhibiting in particular a variation with the orientation angle. Nowadays, an important limitation of this technique lies in the presence of volume scattering, occurring once vegetation is present on the surface, except at large wavelengths such as P-band. Radarclinometry, often also called 'shape-from-shading', and shadow or layover measure (La Prade and Leonardo 1969, Kirscht and Rinke 1998, Simonetto 2002) are the only techniques which need only one single configuration SAR image (and therefore there is very little constraint in terms of data). These techniques are complementary in the sense that the first one is generally used with low slope angles, whereas the other two require high slope values (e.g. greater than $\pi/2$ minus the incidence angle for the shadow reconstruction), limiting their application domain principally to man-made structures, buildings, towers, trees or some cliffs. The cited methods differ by the data needed and the accuracy of the results. In particular, radarclinometry, which is the focus of our interest here, is not the most accurate: our aim was less to compare with other techniques and more to extend the limits of radarclinometry.

Its first application was the Venus DEM map (Willey 1986). Successive works (in particular, Frankot and Chellapa 1988, Guindon 1990, Thomas *et al.* 1991, Paquerault and Maître 1998, Wilson and Hancock 1999, Bors *et al.* 2003) have tried to overcome the main limit of this technique: the geometric ambiguity once we do not assume local cylindricity. Another critical point which meant the technique was not often used, is that the whole surface has generally to be homogeneous and Lambertian. Clearly such an assumption restricts the applicability to large forest areas, such as French Guiana (Amazonia), since it is not valid for bare soil surfaces.

For bare soil, the radar signal depends on surface parameters such as soil moisture and/or soil roughness, as shown by the different backscattering models developed during the past decades: theoretical or empirical (e.g. Fung *et al.* 1992, Oh *et al.* 1992, Dubois *et al.* 1995, Shi *et al.* 1997, Le Hégarat-Mascle *et al.* 2002). Figure 1 shows the backscattering coefficient, σ_0 (in dB) plotted versus incidence angle, in different cases of surface roughness 's' (rms height, Ogilvy 1991) and backscattering mechanisms; in the non Lambertian case, these simulations have been done using the integral equation model (IEM, Fung *et al.* 1992, Zribi *et al.* 1997). It illustrates the importance of the error when not considering the right backscattering diagram in the derivation of the local incidence from observed backscattering value σ_0 . For example, a difference $\Delta\sigma_0$ of +2 dB relative to the 'flat surface' reference backscattering value (for which the incidence angle is around 23°) will be interpreted as due to a local slope of $+6^\circ$ if we consider the $s=0.3$ cm IEM diagram, due to a local slope of $+13^\circ$ if we consider the $s=1$ cm diagram, and cannot be explained using the Lambertian hypothesis.

In this paper, we propose to use backscattering diagrams other than the Lambertian one for the radarclinometry technique. We also propose a way to relax the assumption of homogeneous areas. We apply the proposed approach to arid or semi-arid regions. For this application, we assume that no DEM (even rough) is available. However, the main classes of soil type are easily identified in terms of different soil roughness values.

The paper is organized as follows. Section 2 presents the method: after recalling the radarclinometry principle, the global algorithm adapted to heterogeneous areas, with a known backscattering diagram, is developed. In §3, the method is validated in

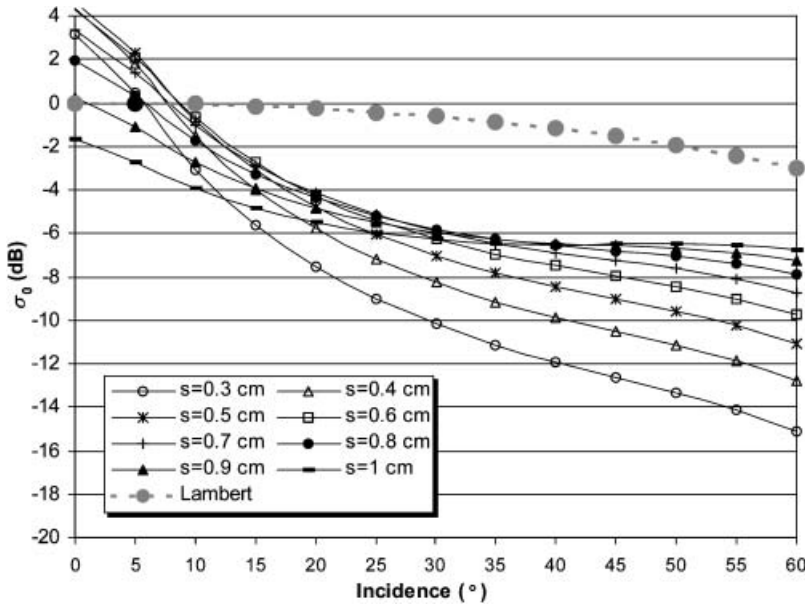


Figure 1. Backscattering coefficient values versus incidence angle, for different kinds of backscattering mechanism and surface. Surface scattering is simulated using the integral equation model.

the case of an Israeli experimental watershed where DEM is known, and then, it is applied in the cases of different Tunisian sites. Section 4 gathers our conclusions.

2. Method

In this section, we present the method used to retrieve soil relief in arid or semi-arid regions. For this specific land surface type, it is not correct to assume that the surface is Lambertian. Moreover the considered areas are heterogeneous, since, for example, the bottoms of the valleys are very smooth surfaces (because of erosion), whereas the relief areas are generally rough (stony) surfaces.

2.1 Radarclinometry principle

Figure 2 shows the geometry of the surface viewing. θ is the incidence angle; x is the distance direction, y the azimuth; α and β are the local angles of the ground relative to x in the xOz plane, and relative to y in the yOz plane; R_d and R_a are the dimensions, respectively in the distance and in the site directions, on a flat ground corresponding to a pixel; and $L(\alpha)$ and $l(\beta)$ are the dimensions of the surface, which depend both on its orientation and on the sensor pixel size on flat ground:

$$L(\alpha) = \frac{R_d \sin \theta}{\sin(|\theta - \alpha|)}; \quad \alpha \in [-\pi/2 + \theta; \theta \cup \theta; +\pi/2] \quad (1)$$

$$l(\beta) \approx \frac{R_a}{\cos \beta}; \quad \beta \in [-\pi/2; +\pi/2] \quad (2)$$

The exact expression of $l(\beta)$ can be found in Petit (2004). Let ΔH_{li} and ΔH_{co} be the altitude differences, respectively, between two consecutive lines and between two

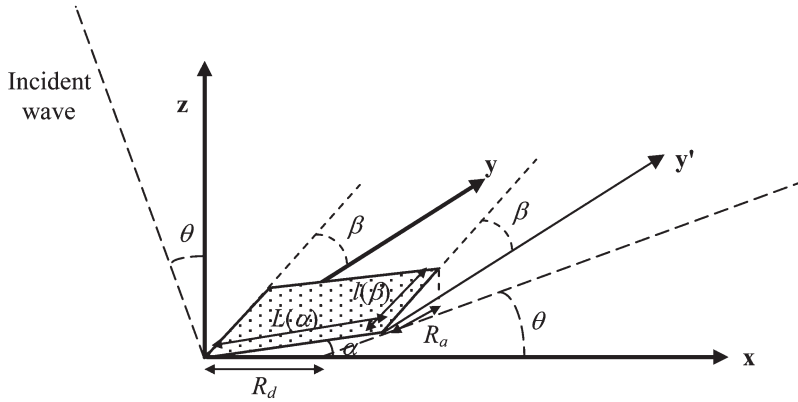


Figure 2. Geometric representation of the radarclinometry main parameters.

consecutive columns of the image. Then, from figure 2, we have:

$$\tan \alpha = \left[\frac{R_d}{\Delta H_{co}} + \frac{1}{\tan \theta} \right]^{-1} \quad (3)$$

$$\tan \beta = \frac{\Delta H_{li}}{R_a} \quad (4)$$

The wave vector is $\mathbf{K} = \begin{pmatrix} -\sin \theta \\ 0 \\ \cos \theta \end{pmatrix}$ and the unit surface normal vector is

$\mathbf{N} = \begin{pmatrix} -\sin \alpha \cos \beta \\ -\sin \beta \\ \cos \alpha \cos \beta \end{pmatrix}$. Thus:

$$\mathbf{K} \cdot \mathbf{N} = \cos(\theta - \alpha) \cos \beta \quad (5)$$

According to the plane wave propagating in free space, the measured power is (e.g. Ulaby *et al.* 1986) P_r :

$$P_r = \frac{P_e G_e G_r \lambda^2}{(4\pi)^3 r^4} \sigma \quad (6)$$

where λ is the wavelength, P_e the emitted power, G_e and G_r the antenna gains, r the distance between the satellite and the target (surface), and σ the product of the equivalent surface by the gain in the backscattering direction. It is called the backscattering coefficient. In the previous works (from Wildey 1986, to Paquerault 1998), the observed surface was assumed to be Lambertian, mainly for simplification. Indeed, it implies that:

$$\sigma = dA \cdot \mathbf{K} \cdot \mathbf{N} \sigma_0 \cos \theta_r \quad (7)$$

where θ_r is the backscattering angle: $\cos \theta_r = \mathbf{K} \cdot \mathbf{N}$, and dA is the resolution surface: $dA = L(\alpha) \cdot l(\beta)$.

The ratio $Q(\theta, \alpha, \beta)$ between the powers backscattered by the observed surface with its orientation angles α and β , and by the same surface but flat is:

$$Q(\theta, \alpha, \beta) = \frac{[\cos(\theta - \alpha)]^2 \cos \beta \sin \theta}{\sin(|\theta - \alpha|) \cos^2 \theta}. \quad (8)$$

However, if the Lambertian assumption may be considered as a first approximation for diffuse scattering surfaces such as dense vegetation, it is not true in most cases where backscattering is dominated by surface scattering. Therefore, here, we develop a more general formulation. In the more general case, we write σ as follows:

$$\begin{aligned} \sigma &= dA(\mathbf{K} \cdot \mathbf{N}) G_s(\theta_r) \\ &= \frac{R_d R_a \sin \theta \cos(\theta - \alpha)}{\sin(|\theta - \alpha|)} G_s(\cos^{-1}[\cos(\theta - \alpha) \cos \beta]) \end{aligned} \quad (9)$$

We deduce the ratio $Q(\theta, \alpha, \beta)$:

$$Q(\theta, \alpha, \beta) = \frac{\cos(\theta - \alpha) \sin \theta}{\sin(|\theta - \alpha|) \cos \theta} \frac{G_s(\cos^{-1}[\cos(\theta - \alpha) \cos \beta])}{G_s(\theta)} \quad (10)$$

A simplification may occur if we suppose that $\beta=0$. This assumption is currently done in a first approximation, and it is justified by the much greater sensitivity of the SAR intensity measurement to the range angle α than to the azimuth angle β (Guindon 1990). Then:

$$Q(\theta, \alpha, 0) = \frac{\sin \theta \cos(\theta - \alpha) G_s(\theta - \alpha)}{\cos \theta \sin(|\theta - \alpha|) G_s(\theta)} \quad (11)$$

G_s can be deduced from electromagnetic simulations of the variation of σ with incidence angle. The integral equation model (IEM) developed by Fung *et al.* (1992) brings a new contribution to the theoretical simulations of backscattering over bare soils. Different experimental studies based on comparison between radar measurements and simulations have shown a large roughness validity domain of this model compared with the other analytical models such as the small perturbation model or Kirchhoff approaches (Rakotoarivony *et al.* 1996, Zribi *et al.* 1997, 2000). In this study, the IEM was used to simulate the backscattering coefficient σ^N in the case of a sized normalized flat surface, i.e. $R_a=R_d=1$ m and $\alpha=\beta=0^\circ$. Then, according to equation (9):

$$G_s(\theta) = \frac{\sigma^N(\theta)}{\cos \theta} \quad (12)$$

Finally, equations (10) and (11) re-write as:

$$Q(\theta, \alpha, \beta) = \frac{\sin \theta}{\sin(|\theta - \alpha|) \cos \beta} \frac{\sigma^N(\cos^{-1}[\cos(\theta - \alpha) \cos \beta])}{\sigma^N(\theta)} \quad (13)$$

$$Q(\theta, \alpha, 0) = \frac{\sin \theta}{\sin(|\theta - \alpha|)} \frac{\sigma^N(\theta - \alpha)}{\sigma^N(\theta)} \quad (14)$$

Equation (14) is used to estimate $|\theta - \alpha|$, as follows. Knowing the values of σ^N versus the local incidence angle (backscattering diagram given by the e.m. model), and knowing, for the considered pixel, the incidence angle θ , and the ratio Q_{obs} between the measured (observed) backscattering value and the corresponding value in the

absence of relief, we deduce $K = Q_{obs} \sigma^N(\theta) / \sin \theta$. Let us consider the function $f(x) = |K \sin(x) - \sigma^N(x)|$, and denote by \hat{x} the value which minimizes $f(x)$. \hat{x} is the researched estimation of $|\theta - \alpha|$, or $(\theta - \alpha)$ if we assume that $\alpha \in [-\pi/2 + \theta; \theta[$. Practically, this latter assumption limits the domain of application of the method, even if theoretically the following step of elevation regularization, which does not use it, can correct the errors in the solution selection ($\alpha = \theta - \hat{x}$ instead of $\alpha = \theta + \hat{x}$).

2.2 Elevation regularization

As said previously, signal variations as a function of β angle are negligible relative to the variations due to the α angle. Therefore, important errors can occur on β estimations, inducing important drifts on elevation estimations. This induces an important line integration effect, visible on the first results. Different ways have then been proposed to force the β angle and help its estimation. They are generally based on a regularization process, which forces the elevation variations to become unimportant, based on the assumption that relief variations are smooth. Regularization also helps to reduce the errors due to speckle (Ulaby and Dobson 1989), which may be important (Guindon 1990).

In this study, three methods of constraining β have been considered.

The first is a minimization of the altitude difference between neighbouring pixels. Indeed, neglecting the β angle in equation (10), α angle and difference elevation dh in the site direction can be known. Then, for each image line, the integration of the dh values gives the elevation relative to a constant $h_0(l)$, which should be estimated for each line. In this first approach, this constant is estimated as the value that minimizes the difference of the elevations between a pixel and its neighbours of previous lines:

$$h_0(l) \text{ is such that } \sum_{s \in \text{line } l} \left(\sum_{s' \in N_s} [h(s) + h_0(l) - h(s')]^2 \right) \text{ minimum} \quad (15)$$

Typically the neighbourhood N_s was equal to few (3 to 10) previous lines and columns. However, results still show a strong line effect. One reason that can be argued, is that the errors occurring in α estimation neglecting β are still not corrected from equation (15). Then, the second approach tested was to perform the difference elevation integration not only according to exact site direction, but also according to directions presenting a few degrees inclination relative to the site direction. In spite of the involved approximation, it leads to good results. Indeed, the different line offsets $h_0(l)$ are thus normalized each one relative to the others, and the difference elevation errors are filtered thanks to the average estimate. Such an approach was also tested with success by Frankot and Chellapa (1988). It is closely akin to the constraint most widely used in shape-from-shading, that is the integrability of the surface: $\partial^2 h / \partial x \partial y = \partial^2 h / \partial y \partial x$.

The third method of elevation regularization is based on a classical Markovian approach. According to Paquerault (1998), we introduce in the minimization an energy neighbourhood term depending on the altitude differences between a given pixel and its neighbours:

$$U_{\Delta h}^{(k)}(s) = \sum_{s' \in N_s} \left[h^{(k)}(s') - h^{(k)}(s) \right]^2 \quad (16)$$

where (k) is the iteration number, s the considered pixel, s' another pixel belonging to s neighbourhood N_s , and $h(\cdot)$ the altitude function. We note that a constraint on α and β regularity, corresponding to an assumption of regular slope rather than a weak slope, was also tested. We only mention it here since, on the considered application, it showed poorer performance than the regularization on h . A possible explanation is that a constraint of regularity on (α, β) propagates the angle estimation errors, whereas the h constraint forces weak slope values; that is after all the more current case.

Now, if the 'data attachment' term is written:

$$U_0^{(k)}(s) = \min \left\{ Q_{obs} - \frac{\sin \theta}{\sin(|\theta - \alpha^{(k)}|) \cos \beta^{(k)}} \frac{\sigma^N \left[\cos^{-1} \left(\cos(\theta - \alpha^{(k)}) \cos \beta^{(k)} \right) \right]}{\sigma^N(\theta)}, \xi \right\} \quad (17)$$

where $\alpha^{(k)}$ and $\beta^{(k)}$ are the angle estimates at the iteration (k) , and ξ is a threshold value to limit the values taken by this 'data attachment' term, even in the case of strong speckle effect.

The global energy is:

$$U^{(k)} = \sum_s U_0^{(k)}(s) + v U_{\Delta h}^{(k)}(s) \quad (18)$$

where v is a relative weighting coefficient between the two energy terms.

The minimization of $U^{(k)}$ can be achieved using a simulated annealing algorithm as in Paquerault (1998), or by a local minimization method; even if theoretically the simulated annealing should lead to the global minimum, in practice, it often achieves only local minimum (Paquerault 1998). Practically, at each image pixel s , a new value of height $h(s)$ is tested, from which are deduced $U_{\Delta h}(s)$, the $\alpha(s)$ and $\beta(s)$ angles, $U_0(s)$, and $U^{(k)}$. If the tested height value is satisfying, e.g. it implies a smaller value of U than previously, the height, angles and energy values are updated accordingly, otherwise they are left unchanged. The algorithm is stopped when no change is accepted during a given number of iterations.

2.3 Classification process and regularization

To compute the ratio Q_{obs} , which approximates $Q(\theta, \alpha, \beta)$ (equation 13), or $Q(\theta, \alpha, 0)$ (equation (14)), we need to know the backscattered signal by the considered area in the absence of relief. This signal is generally unknown, and it is often taken to be equal to the mean value of the backscattered intensities over the whole image. This may induce strong mistakes either in the case of inhomogeneous areas, i.e. areas containing different backscattering classes, or if the relief induces a not negligible bias on the mean signal value, e.g. if the area shows an averaged slope significantly different from zero.

Here, we propose to use rather a classification process to determine the equivalent 'flat area' backscattered signal. We consider a small number of classes, typically three, whose features can easily be estimated from selected areas in a supervised way. Ground data is not necessary, since for such a number of classes, it is not difficult to find representative and approximately flat areas on the image. In particular, in the case of semi-arid or arid regions, the bottoms of the valleys and the upper plateaux can be identified. Figure 3 shows a SAR image acquired over the Israeli test site used in §3 for validation. The class learning areas are shown. Class 1

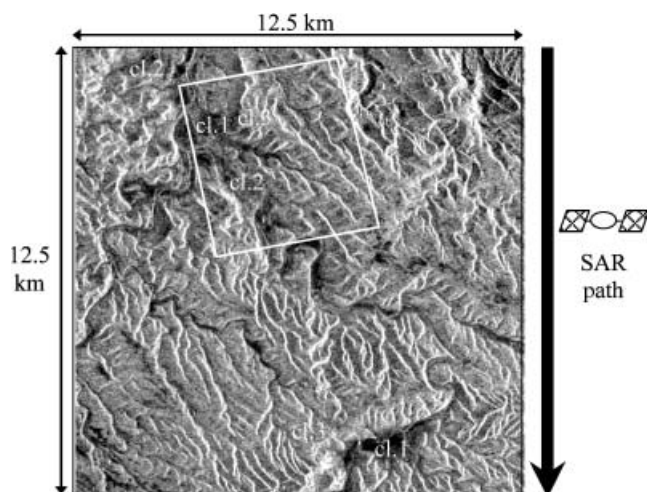


Figure 3. ERS/SAR image of the Israeli site, showing the DEM ground data area and the selected areas for class feature learning.

corresponds to the very bottom of the valleys, class 3 the upper plateaux and class 2 is intermediate. Figure 4 shows three photographs of the surface corresponding to these classes. Since, due to natural erosion, roughness generally decreases from plateaux to valleys, we expect the three classes to exhibit increasing signal (intensity) values.

Knowing the class features, the first classification performed is a simple minimum distance classification, i.e. in every pixel the decided class label is that minimizing the Euclidian distance between the observed backscattering value in dB and the class centre also in dB. From this classification, the Q_{obs} values can be obtained for every pixel. The first estimation of the digital elevation model can therefore be computed and regularized as explained in §2.2.

Then, from this first DEM estimation, a new classification is performed. Indeed, in the relief areas, the slope can modify the backscattering value such that an error occurs in the minimum distance classification process. In other words, because of the relief, the radiometric (and neighbourhood) information may be not sufficient to determine the pixel class. Here, we propose to help classification using altitude information also. In particular, we introduce a ‘constraint’ term for the two classes ‘bottom of the valleys’ and ‘upper plateaux’.



Figure 4. Photos of the surface corresponding to the three classes, having decreasing soil roughness value from ‘upper plateaux’ to ‘bottom of the valleys’, considered on the Israeli site. The size of the reference square is 1 m².

Using a classical *maximum a posteriori* criterion (e.g. Duda and Hart 1973, Geman and Geman 1984), the label image L is estimated from the data X and the assumed probability laws, conditional and *a priori*:

$$L = \operatorname{argmax}_{L'} P(X/L')P(L') \quad (19)$$

Using a Markovian assumption and the equivalence between Markov random fields (MRF) and Gibbs ones, the *a priori* probability $P(L')$ is written as an exponential of an energy term, itself defined from the cliques potential in a neighbourhood around each considered pixel. Now, if the conditional probability $P(X/L')$ can be assumed to be Gaussian, it is also proportional to an exponential, and the maximization of the probability *a posteriori* is given by the minimization of the argument of the exponential, i.e. in every pixel the minimization of the sum of a ‘data attachment’ term $U_{data}^{(k)}(s)$ and a ‘neighbourhood’ term $U_N^{(k)}(s)$:

$$L = \operatorname{argmin} \left\{ \sum_s U_{data}^{(k)}(s) + U_N^{(k)}(s) \right\} \quad (20)$$

$$U_{data}^{(k)}(s) = \frac{[I^{(k)}(s) - \bar{I}^{(k)}(s \text{ class})]^2}{2\operatorname{var}^{(k)}(I(s \text{ class}))} \quad (21)$$

$$U_N^{(k)}(s) = \frac{c_n}{2} \sum_{s' \in N_s} [1 - \delta(s \text{ class}, s' \text{ class})] \quad (22)$$

where the superscript (k) denotes the current iteration since convergence is iterative, s is the considered pixel and ‘ s class’ its class, $\bar{I}(s \text{ class})$ and $\operatorname{var}(I(s \text{ class}))$ are the mean and the variance of s class image value, i.e. radiometric intensity I in dB, and $\delta(i, j)$ is the Kroenecker symbol, which is equal to 1 if $i=j$, and equal to 0 otherwise, c_n is the weighting factor between the ‘data attachment’ and ‘neighbourhood’ terms. In our case, all the classes are assumed to have the same variance, so that it does not have an impact on the minimization.

Now, to introduce altitude information, let us consider that the data feature vector is constituted not only by the intensity value but also by the altitude estimation. Then, based on a Gaussian assumption for the conditional distribution of the altitudes relative to their class, we define the following energy term:

$$U_{cl}^{(k)}(s) = \frac{[h^{(k)}(s) - \bar{h}^{(k)}(s \text{ class})]^2}{2\operatorname{var}^{(k)}(h(s \text{ class}))} \quad (23)$$

where $\bar{h}(s \text{ class})$ is the altitude average over s class, and $\operatorname{var}(h(s \text{ class}))$ its variance. To achieve greater robustness, these two statistical moments are not computed on the whole image, but on sub-areas (typically 100×100 pixels). Considering that the new data are vectorial: $(I^{(k)}(s) \ h^{(k)}(s))^t$, with diagonal covariance matrix, the new ‘data attachment’ term is the sum of $U_{data}^{(k)}(s)$ and $U_{cl}^{(k)}(s)$, respectively, defined by equations (21) and (23). Now, taking into account the altitude only in the case of the classes for which it is relevant, such as ‘bottom of the valleys’ and ‘upper plateaux’, is done by assuming an infinite variance for all other classes. In the same spirit, it can also be useful to introduce a weighting factor c_c between the ‘intensity data attachment’ and the ‘altitude’ one.

Finally, the global energy that should be minimized is then the weighted sum of three terms over all the image pixels:

$$U^{(k)} = \sum_s U_{data}^{(k)}(s) + c_c U_{cl}^{(k)}(s) + \frac{c_n}{2} U_N^{(k)}(s) \quad (24)$$

where c_c and c_n are weight coefficients.

The global minimization is iterative, and as previously, it can be achieved using a simulated annealing algorithm. Figure 5 summarizes the proposed algorithm.

3. Application to SAR/ERS data

To validate the algorithm presented in §2, different sites have been studied, in Israel and in Tunisia. All the data have been acquired during the dry season (from April to September) to avoid any soil moisture effect on the radar signal. The data were acquired by the SAR of ERS-1 and ERS-2 (Earth Remote Sensing satellites). This SAR operates at C band (5.3 cm wavelength), VV polarization, and incidence angle centred on 23°. The pixel size of 'PRrecision Images' (PRI) is 12.5 m × 12.5 m; however its spatial resolution is 25 m × 25 m. Therefore, and to reduce speckle effect, we perform a 2 × 2 pixels spatial average, leading to a pixel size of 25 m × 25 m. Due to the pixel correlation, the variance is reduced by a factor L_{eq} lower than the value expected in the uncorrelated case, namely 4.

Speckle has also been reduced by performing a multitemporal averaging when we had several images acquired at different dates. The exact number of available images depends on the considered site; it ranges from 3 to 5. Table 1 shows the main features of the considered sites within the different SAR/ERS PRI images: size of the studied area, number of SAR images available and used in the multitemporal and dynamic range of the central pixel incidence and looking angles when considering the different images. For a given site, all the considered images have been acquired in the same geometry: same frame and same track. Therefore, first the looking angle dispersion (as shown in table 1) is small, and there is a simple translation between the couple of images. The translation vectors are found by maximization of the correlation. Thanks to the same geometry of acquisition, the precision of the image superposition is generally better than 1 pixel both in the line and the column directions.

3.1 Case of the Israeli site

The described algorithm (cf. figure 5) has been applied to the ERS/SAR data of the Israeli site in the Negev desert (Avdat). Besides, for comparison, we have also computed the results when using only minimum distance classification (no regularization under altitude constraint), and the results obtained with homogeneous area assumption (no classification) and estimation of the flat area signal by averaging over the whole image.

Let us start the analysis of the results by the examination of the α angle maps. This parameter is certainly the most important parameter for signal correction (of the relief effect), and for DEM derivation. Figure 6(a–c) shows the obtained maps of α , (a) based on the assumption of homogeneous area, (b) using minimum distance classification (MDcl), (c) using altitude constrained classification (ACcl). We note that figure 6(a) is very close to figure 3. Indeed, any signal variation has been reported on the α angle. This is not correct since the bottoms of the valleys exhibit

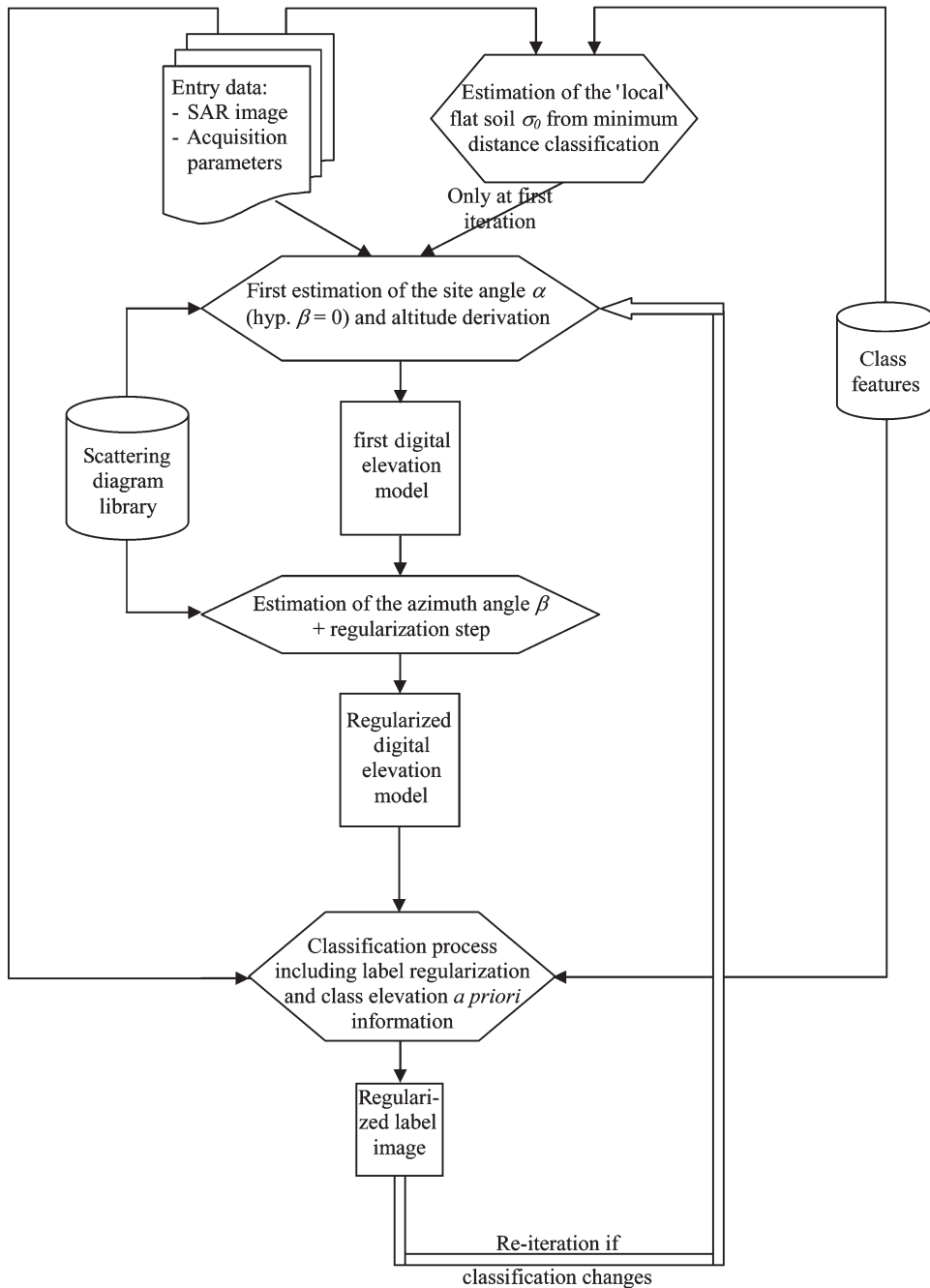


Figure 5. Proposed algorithm to retrieve relief in the case of inhomogeneous regions.

very low α values (to -30°), instead of about null values. This appears clearly on the image part surrounded by a circle.

In the case of the figure 6(b) α map, the darkest areas of figure 6(a) do not necessarily have the lowest α values, since some of them have been classified in the 'bottoms of the valleys' class (the class patchwork is visible in the example pointed

Table 1. Main features of the considered sites in the different SAR/ERS PRI images.

Site	Israel	Tunisia no.1	Tunisia no.2	Tunisia no.3
Size in SAR PRI pixels	1000 × 1000	1000 × 1000	1000 × 1000	1000 × 1000
Number of images available	5	3	3	3
Range of the central incidence angle	[20.26°; 20.42°]	[25.13°; 25.19°]	[24.42°; 24.47°]	[21.56°; 21.61°]
Range of the central looking angle	[20.00°; 20.16°]	[24.80°; 24.87°]	[24.10°; 24.16°]	[21.30°; 21.34°]

out by the circle on the image). The corresponding classification result is shown in figure 6(d). With further examination, some classification errors come to light. For example, in the circled area, the ‘bottoms of the valleys’ class is too much extended in the right and right-top direction, which prevents the retrieval of the descent from the relief pointed by the triangle. In the case of figure 6(c), such errors seem to have been corrected thanks to the improvement of the classification (shown in figure 6(e)). The comparison of figure 6(d) and (e) puts forward the evolution of the classification due to the altitude term (equation 24): decrease of the ‘upper plateaux’, previously overestimated, and increase of the two other classes; in particular, the new areas of the class ‘bottom of the valleys’ are validated from qualitative photointerpretation of the SAR image.

Figure 6(f), (g) and (h) shows the DEM results respectively obtained (f) based on the assumption of homogeneous area, (g) using MDcl, (h) using ACcl. The histograms of these images have also been plotted. Table 2 gives the main statistical parameters corresponding to these different DEM. We also add, for comparison, the results obtained using the Lambertian model. We note that in the case of the homogeneous area, the dynamic range and the standard deviation of the DEM are much greater than in the case of the use of a classification map. This is an unsurprising result since, in this case, all the signal variations have been reported on the DEM, in contrast to the 3-class case where some of these variations are explained by class changes. Comparing the results obtained with the two classification processes, figure 6(g) seems more detailed than figure 6(h). However, this is rather an effect due to the dynamic ranges (cf. table 2).

Looking more precisely, figure 6(g) appears to contain more errors than figure 6(h). Some examples have been shown in figure 7. On the SAR image, we easily recognize the bottoms of the valleys and the main relief. On the first example, the MDcl DEM shows an error in the left-bottom part of the area, where a bottom of valley is misinterpreted as a relief; this does not occur on the ACcl DEM. On the second example, the very bright structure at the centre of the area should in fact have been a valley bottom. Once more this error on the MDcl DEM is corrected on the ACcl DEM. On the third example, the problem with the MDcl DEM is that the relief in the top left to centre part of the area is not retrieved: DEM takes low values (dark pixels), which is not the case with the ACcl DEM. In these examples, we see that many MDcl DEM errors are removed on the ACcl DEM. However, we note that the ACcl DEM also shows its own remaining errors.

Figure 8 shows four examples of profiles of altitude estimation error (in absolute value), selected within the sub-area where ground DEM is known. The parallelepiped plotted on figure 3 indicates the area where a 25 m DEM is available.

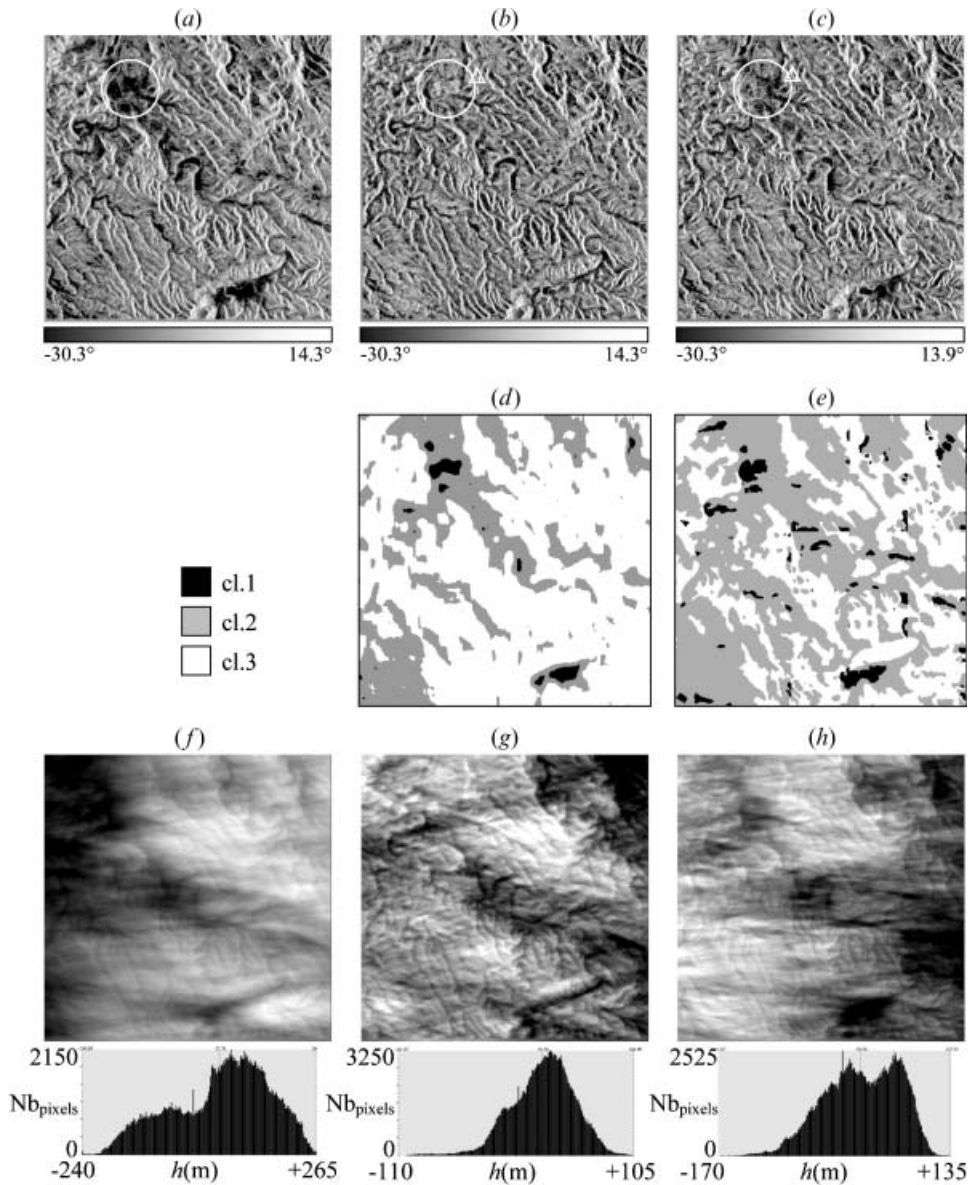


Figure 6. Results for the Israeli site: (a–c) α angle estimation, respectively (a) based on the assumption of homogeneous area, (b) using minimum distance classification (MDcl), (c) using altitude constrained classification (ACcl); (d–e) classification results, (d) MDcl and (e) ACcl (class centres are equal to -10 dB, -7 dB and -5 dB); and (f–h) DEM results, obtained respectively from (f) homogeneous area assumption, (g) MDcl, (h) ACcl.

The DEM has been projected in the SAR geometry. For each profile, four plotted altitude errors are shown, corresponding to each of the DEM retrieval methods: ACcl, MDcl, using the homogeneous area assumption, and using the Lambertian assumption. We clearly see on these examples that neither the Lambertian assumption, nor the homogeneous area can lead to satisfying results. Concerning ACcl and MDcl, they are generally very close. On profile 1, the first 50 m are a

Table 2. Main statistical parameters corresponding to different DEM obtained on the Israel site.

Altitude statistics (m)	Dynamic range	Median value	Mean value	Standard deviation
Homogeneous area assumption	507.2	73.5	57.8	104.6
Minimum distance classification	216.0	23.5	21.5	28.9
Constrained DEM classification	319.5	25.3	23.3	48.1
Lambertian diffusion model	599.93	92.1	99.7	110.7

plateau according to MDcl DEM, and a valley according to ACcl DEM, which is the correct result. On profile 2, the two estimations of DEM are very close, ACcl estimation slightly better at the beginning of the profile and between the 100th and 120th pixel of the profile. On profile 3, the two DEMs show important errors at the beginning and at the end of the profile; however, between 50 and 100 m, the ACcl DEM shows results much closer to the ground DEM variations. Finally, in the case of profile 4, the two DEM are close except for the pixels belonging to the interval [0,50] and [100,130] where the improvement due to ACcl is visible. In conclusion, the examination of the profiles allows us to globally validate both DEM estimations from ACcl or MDcl, and to show the slightly better performance of the ACcl DEM.

Table 3 gives the global quantitative errors relative to the entire ground data DEM area. We note that the Lambertian model results exhibit large errors for the altitude as well as for the angles α or β . Introducing the right backscattering diagram slightly reduces the errors until classification is performed. Finally, altitude errors

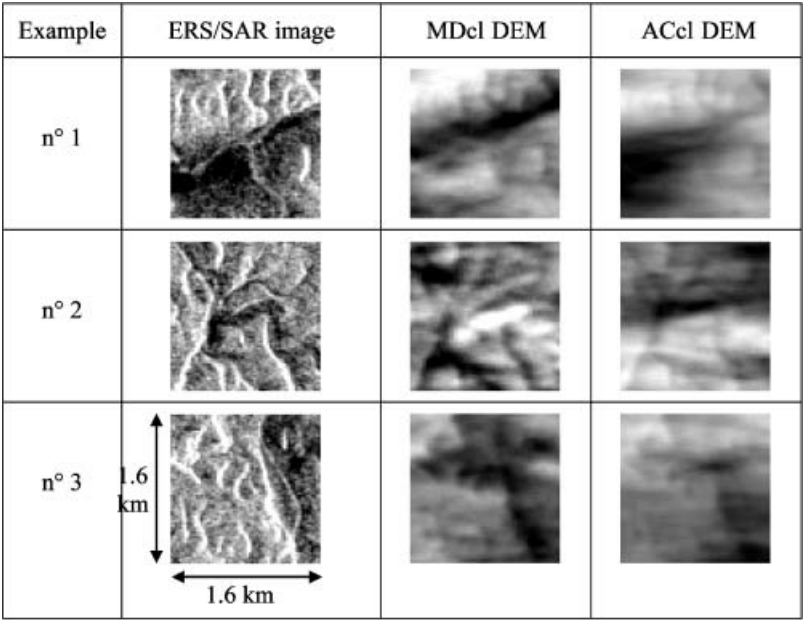


Figure 7. Three examples of sub-areas on the Israeli site showing: the ERS/SAR sub-image, the DEM obtained using the minimum distance classification (MDcl DEM), and the DEM obtained using the altitude constrained classification (ACcl DEM).

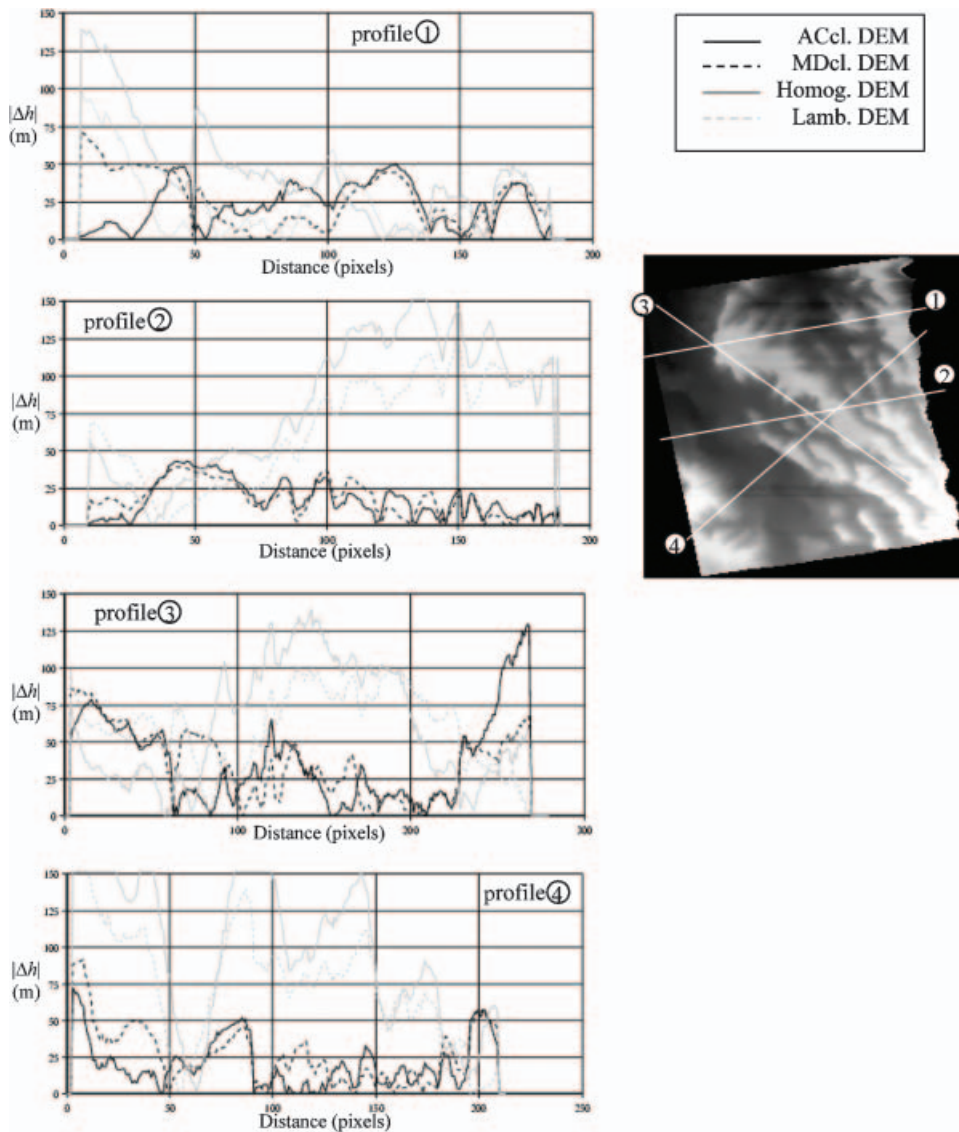


Figure 8. Four examples of profiles of altitude estimation error in absolute value ($|\Delta h|$) for the Israeli site. For each profile, the four plotted curves correspond to the four DEM retrieval methods: altitude constrained classification (ACcl DEM), minimum distance classification (MDcl DEM), using the homogeneous area assumption (Homog. DEM), and using the Lambertian assumption (Lamb. DEM). The location of the profiles is plotted on the DEM image, represented after projection in the SAR geometry.

are divided by a factor around 2 for altitudes, and 1.5 for angles. Rather surprisingly, the results are slightly better with minimum distance classification than with altitude constrained classification. In fact, this is mainly due to an important error in the bottom part of the DEM area, as shown in figure 9(a). In comparison, such an error is not present with the MDcl method (cf. figure 9(b)). If we do not consider this area, we find again that the results are very close, slightly better in the ACcl case.

Table 3. Statistical parameters of the comparison of the different DEM computed on the Israel site with the ground DEM.

Errors=absolute difference	Altitude (m)			α angle (°)			β angle (°)		
	Median	Mean	Std dev.	Median	Mean	Std dev.	Median	Mean	Std dev.
Homogeneous area hypothesis	49.1	58.7	43.1	2.27	2.83	2.38	3.14	3.88	3.13
Minimum distance classification	24.2	28.9	21.0	1.44	2.26	2.33	1.93	2.71	2.53
Altitude constrained classification	29.4	35.4	27.5	1.86	2.60	2.44	2.63	3.42	2.93
Lambertian diffusion	56.0	70.9	60.2	2.69	3.31	2.77	4.03	4.88	3.71

3.2 Case of the Tunisian site

In this section, we aim at validating the proposed methodology on some other sites. These sites are located in the south of Tunisia, close to the Sahara. Unfortunately, in Tunisia, there are no DEM ground data to validate our results. Therefore our validation will be only qualitative.

Figure 10 shows the first Tunisia site, located in the centre of Tunisia. On the ERS/SAR image (be aware of the satellite path on the left of the image), we recognize a plain on the upper left of the area, and then some cliffs bordering a more mountainous region. Three classes ranging from plain to mountainous areas have been selected. From supervised learning areas, we find that their intensity values are, respectively, centred on -11.5 , -10.5 and -9.5 dB. These intensity values are much lower than those found in the Israeli case (respectively, -10 dB, -7 dB and -5 dB). Indeed, the studied sites in Tunisia are much less stony and rocky than the Israeli site. Therefore, soil roughness is generally low, which both explains the observation of lower intensity values, and induces the choice of a smaller rms value backscattering diagram. In figure 10, we have represented two profiles in the SAR image geometry. The arrows point at the main relief on the SAR image, and their corresponding points on the profile. We note the good correspondence between both. The altitude dynamic range length (the maximum altitude minus the

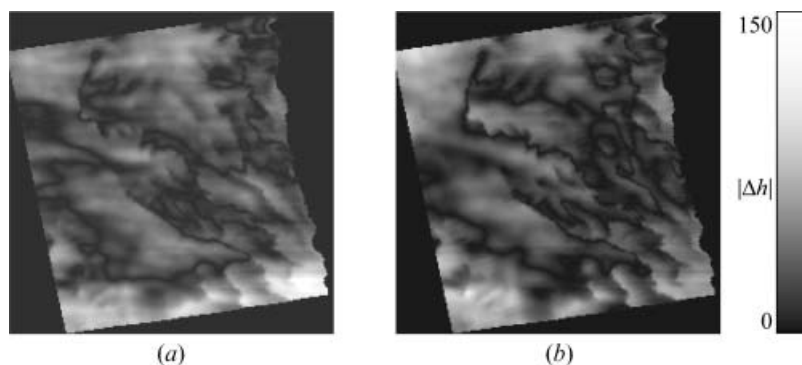


Figure 9. Image of the altitude estimation error in absolute value ($|\Delta h|$) for the Israeli site, (a) the ACcl DEM and (b) the MDcl DEM.

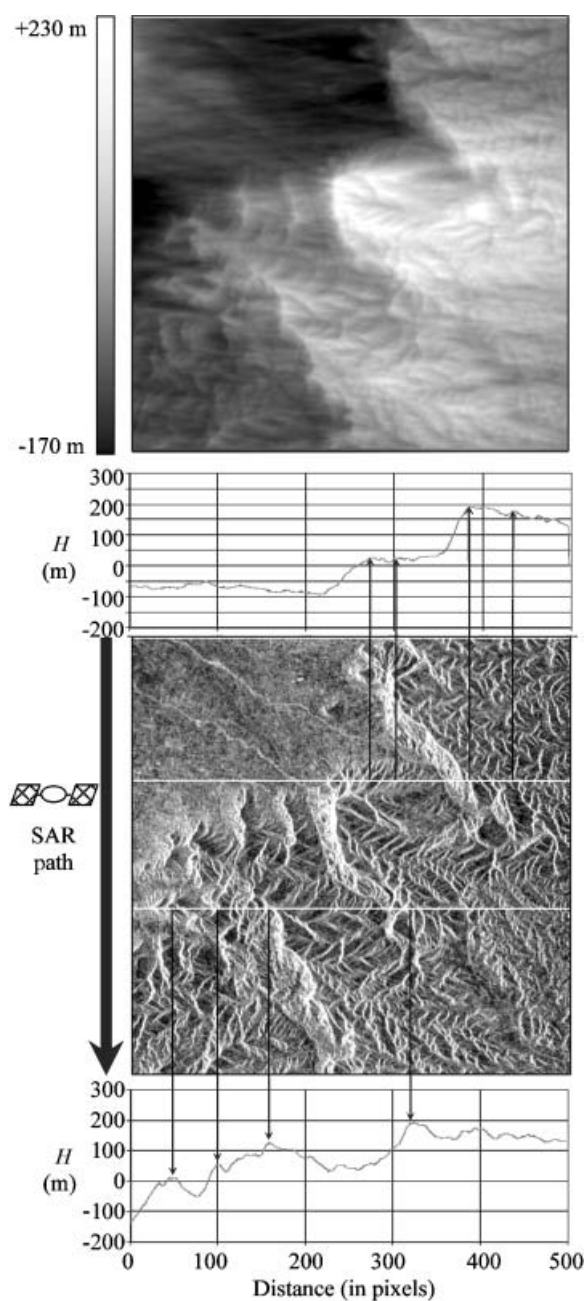


Figure 10. First Tunisia site: retrieved DEM (upper image), SAR image (lower image), and two DEM profiles put in correspondence with the SAR image.

minimum), around 350 m, is also consistent with the *a priori* knowledge of the region.

Figure 11 shows the second Tunisia site. The global ERS/SAR image is the same as those from which we extracted the data for the first site. However this second site is very different. It is also located in the centre of Tunisia, but more southern than

the first one. We recognize a valley (dark areas) surrounded by relief. It seems also that there is a plateau on the left part of the area, which leads to the valley, whose outlet is on the right middle of the image. Three classes respectively centred on -12.5 , -9.5 and -8.0 dB have been selected. In figure 11, we have represented two profiles in the SAR image geometry, and put them in correspondence with the main relief on the SAR image. As previously, we note the globally good

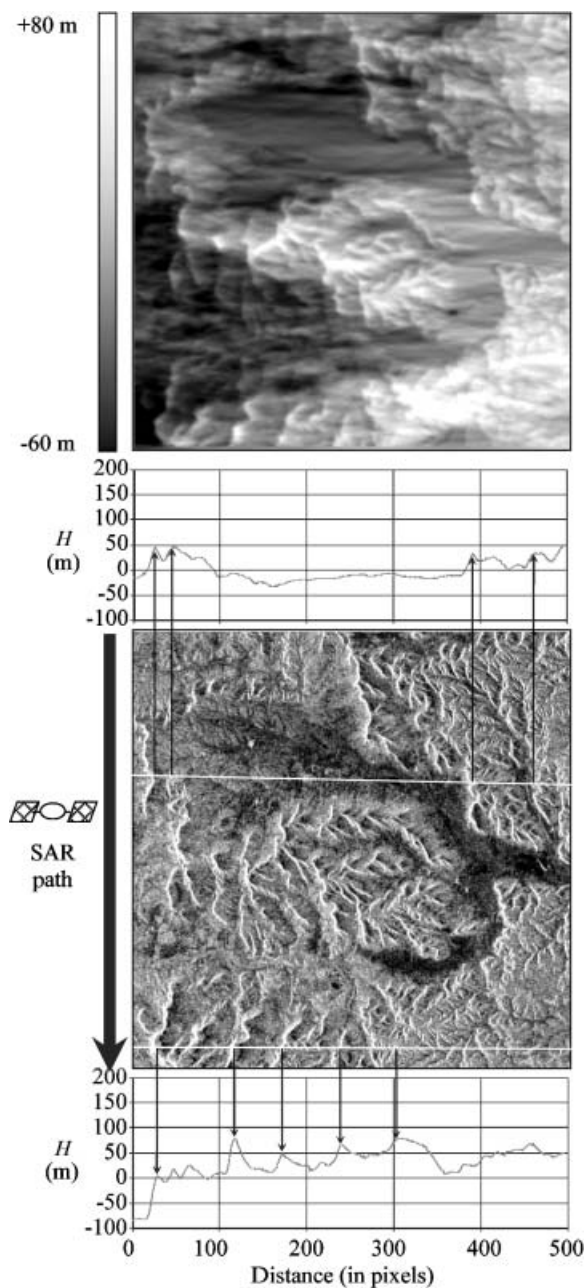


Figure 11. Second Tunisia site: retrieved DEM (upper image), SAR image (lower image), and two DEM profiles put in correspondence with the SAR image.

correspondence. The less satisfying points are first the fact that the global incline of the valley is not in the right direction (however the error remains within the order of magnitude of the errors encountered in the Israeli case: 30 m); second, the line integration effect has not been completely removed on the valley area. The altitude dynamic range length is around 200 m, which is smaller than in the previous example Israeli site and the first Tunisian site. In fact, we think that, with the method that we developed, there is an irreducible residual error (in absolute value) in the DEM retrieval, which is more visible as the global difference altitude is not high. This will be confirmed by the third example.

Figure 12 shows the third Tunisian site. It is very different from the other two, since it is mainly sand dunes. It is located on the border of the Sahara. The three classes selected are respectively centred on -15 (dunes), -10 and -8.5 dB. With this example, we see that we reach the limits of the applicability of the method. Even if the main dunes are roughly located, many errors occur. First, flat areas between sand dunes are not so flat (according to the retrieved DEM). Second, in several cases, only one side of the sand dune is recognized. Indeed, the dune side turned towards the SAR sensor (be aware of the location of the SAR on the right of the image) has a signal very close to the rough areas between dunes, and the algorithm is not able to correct all the initial classification errors (even if the result is strongly improved relative to those obtained with the MDel classification). This induces major mistakes in the DEM. Moreover, the backscattering surface model is insufficient to simulate the radar signal because of the large volume diffusion occurring in the case of sand dunes.

4. Conclusion

The aim of this work was to extend radarclinometry technique to regions where the two current assumptions, (i) Lambertian backscattering, and (ii) homogeneous areas, are not possible. Examples of such regions are the arid or semi-arid areas. Moreover, for these regions, DEMs are still not very precise, and their knowledge is important for radar signal measurement interpretation, for example for geophysical parameters such as aerodynamic roughness retrieval (e.g. Greeley and Blumberg 1995, Le Hégarat-Masclé *et al.* 2003).

In this paper, we have shown that using a backscattering diagram provided by theoretical models, such as the IEM, adapted to the considered surface (its roughness in particular), and determining roughly the different kinds of area present on the site by classification, allows good retrieval of the DEM. We also propose to refine the algorithm by introducing an altitude constraint in the classification process. In this version of the algorithm, DEM map and class map are thus determined simultaneously in an iterative process.

Four different sites have been considered for validation. The first one is located in Israel and it allows quantitative validation because a DEM is available. The three others are located in Tunisia, and validation was qualitative. These four sites represent four different kinds of arid or semi-arid region: more or less stony, with mountainous areas, very smooth valleys and sand dunes. The results are rather convincing. The global difference elevation is consistent with ground knowledge, the main relief structures are well recognized, and the bottoms of the valleys are about flat. Quantitatively, the comparison with the ground data DEM in the case of the Israeli site shows that the altitude absolute error is around 30 m, corresponding to a relative error of about 10%, the site angle (α) absolute error is around 2.5° , and the

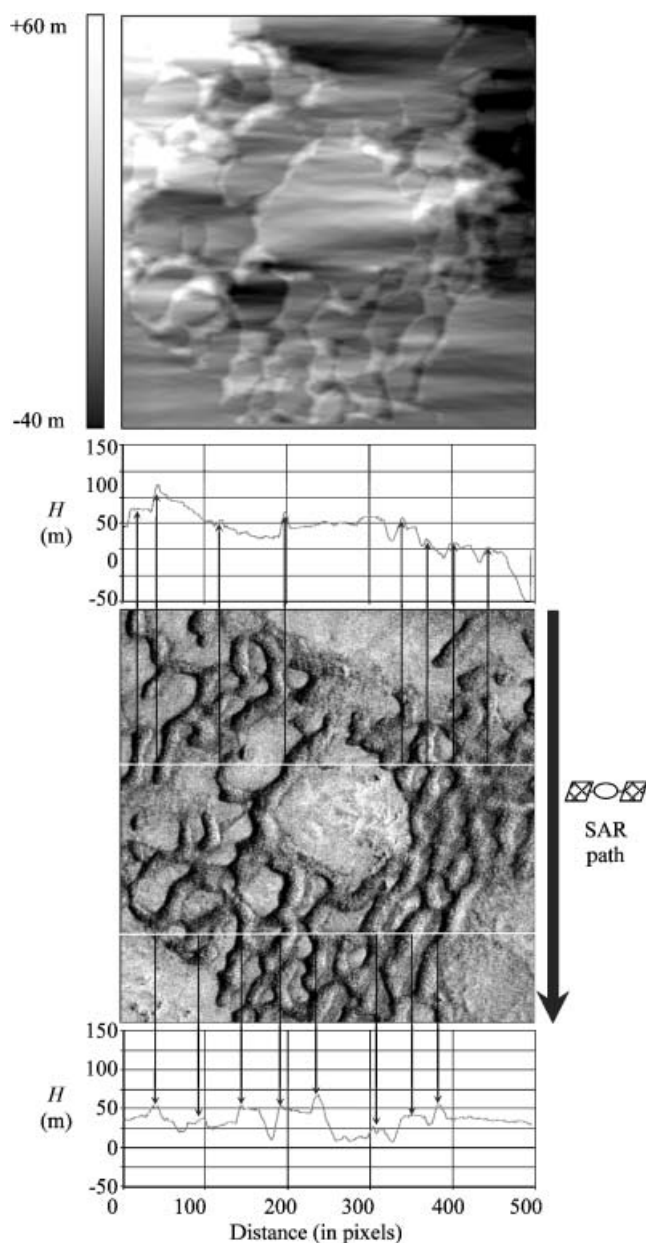


Figure 12. Third Tunisia site: retrieved DEM (upper image), SAR image (lower image), and two DEM profiles put in correspondence with the SAR image.

site angle (β) absolute error is around 3.0° . This corresponds to errors on the SAR signal ranging from 2 dB for the very smooth surfaces and low incidence angles, to 1 dB for smooth surfaces at low incidences or very smooth surfaces at incidences greater than 30° , or less than 0.5 dB for either rough surfaces or high incidence angles. Now, knowing that the ERS/SAR calibration error can reach 1 dB, the obtained accuracy in the slope angles retrieval appears sufficient for data relief effect

correction. The analysis of the effect of this correction on the accuracy of geophysical parameter retrieval can then constitute future work.

Only the case of the site with sand dunes is less satisfying. Now, several problems remain and, for better results, one should probably introduce more physical information, such as the fact that a dune has two sides. The backscattering diagram should also be more specific because of the specific volumetric diffusion.

In conclusion, this study states the importance of considering the correct backscattering diagram and class feature for radarclinometry performance. It also seems that, due to the specificities of radar imagery (speckle, geometry), there is a limit in performance. Including in the process some points where the altitude is *a priori* known could perhaps help to overcome this. An alternative could be to use radarclinometry in collaboration with radarpolarimetry. In this case, the required data are polarimetric, and each slope angle is estimated using the technique that is more sensitive to it: radarclinometry for the site angle and radarpolarimetry for the azimuth angle.

Acknowledgments

The data were acquired in the framework of the FLAUBERT (FLood in Arid Unit By Earth Remote Techniques) project, supported by the European Community DGXII. We also thank Eilon Adar (Ben Gurion University) for ground data and the referees for their useful comments.

References

- BORS, A., HANCOCK, E.R. and WILSON, R.C., 2003, Terrain analysis using radar shape-from-shading. *IEEE Transactions on Pattern Analysis and Machine Intelligence*, **25**, pp. 974–992.
- DUBOIS, P., VAN ZYL, J. and ENGMAN, T., 1995, Measuring soil moisture with imaging radars. *IEEE Transactions on Geoscience and Remote Sensing*, **33**, pp. 915–926.
- DUDA, R. and HART, P., 1973, *Pattern Classification and Scene Analysis* (New York: John Wiley & Sons).
- FRANKOT, T.R. and CHELLAPA, R., 1988, A method for enforcing integrability in shape from shading algorithms. *IEEE Transactions on Pattern Analysis and Machine Intelligence*, **10**, pp. 439–451.
- FUNG, A.K., LI, Z. and CHEN, K.S., 1992, Backscattering from a randomly rough dielectric surface. *IEEE Transactions on Geoscience and Remote Sensing*, **30**, pp. 356–369.
- GABRIEL, A.K. and GOLDSTEIN, R.M., 1988, Crossed-orbit interferometry: theory and experimental results from SIR-B. *International Journal of Remote Sensing*, **9**, pp. 857–872.
- GEMAN, S. and GEMAN, D., 1984, Stochastic relaxation, Gibbs distribution and Bayesian restoration of images. *IEEE Transactions on Pattern Analysis and Machine Intelligence*, **6**, pp. 721–741.
- GREELEY, R. and BLUMBERG, D.G., 1995, Preliminary analysis of Shuttle Radar Laboratory (SRL-1) data to study aeolian features and processes. *IEEE Transactions on Geoscience and Remote Sensing*, **33**, pp. 927–933.
- GUINDON, B., 1990, Development of a shape-from-shading technique for the extraction of topographic models from individual spaceborne SAR images. *IEEE Transactions on Geoscience and Remote Sensing*, **28**, pp. 654–661.
- KIRSCHT, M. and RINKE, C., 1998, 3D reconstruction of buildings and vegetation from SAR images. *Proceedings of IAPR Workshop on Machine Vision Applications, Makuhari, Chiba (Japan), 17–19 November 1998*, pp. 228–231.
- LA PRADE, G. and LEONARDO, E., 1969, Elevation from radar imagery. *Photogrammetric Engineering*, **35**, pp. 366–371.

- LEBERL, F., 1979, Accuracy analysis of stereo side looking radar. *Photogrammetric Engineering and Remote Sensing*, **45**, pp. 1083–1096.
- LEE, J.S., SCHULER, D.L., AINSWORTH, T.L., KROGAGER, E., KASILINGAM, D. and BOERNER, W.M., 2002, On the estimation of radar polarization orientation shifts induced by terrain slopes. *IEEE Transactions on Geoscience and Remote Sensing*, **40**, pp. 30–41.
- LE HÉGARAT-MASCLE, S., ZRIBI, M., ALEM, F., WEISSE, A. and LOUMAGNE, C., 2002, Soil moisture estimation from ERS/SAR data: Toward an operational methodology. *IEEE Transactions on Geoscience and Remote Sensing*, **40**, pp. 2647–2658.
- LE HÉGARAT-MASCLE, S., ZRIBI, M., MARTICORENA, B., BERGAMETTI, G., KARDOUS, M., CALLOT, Y., CHAZETTE, P. and RAJOT, J.-L., 2003, Use of ERS/SAR measurements for soil geometric and aerodynamic roughness estimation in semi-arid and arid areas. *IGARSS '03*, Toulouse, France, 20–25 July, CDROM.
- MASSONNET, D. and RABAUTE, T., 1993, Radar interferometry: limits and potential. *IEEE Transactions on Geoscience and Remote Sensing*, **31**, pp. 455–464.
- Ogilvy, O., 1991, *Theory of Wave Scattering from Random Rough Surfaces* (Bristol: Adam Hilder).
- OH, Y., SARABANDI, K. and ULABY, F.T., 1992, An empirical model and an inversion technique for radar scattering from bare soil surfaces. *IEEE Transactions on Geoscience and Remote Sensing*, **30**, pp. 370–381.
- PAQUERAULT, S., 1998, Restitution du relief à partir d'images radar par radarclinométrie. PhD thesis of the ENST, n° ENST 98 E 007.
- PAQUERAULT, S. and MAÎTRE, H., 1998, A new method for backscatter model estimation and elevation map computation using radarclinometry. *EUROPTO-SPIE Conference, SAR Image Analysis, Modeling and Techniques, Barcelona, Spain, 23–24 September 1998*, in *Proceedings of the International Society for Optical Engineering*, vol. 3497.
- PETIT, D., 2004, Reconstruction du 3D par interférométrie radar à haute résolution. PhD thesis of the University Toulouse 3, France.
- RAKOTOARIVONY, L., TACONET, O., VIDAL-MADJAR, D. and BELLEMAIN, P., 1996, Radar backscattering over agricultural bare soils. *Journal of Electromagnetic Waves and Applications*, **10**, pp. 187–209.
- SCHULER, D.L., LEE, J.S. and DE GRANDI, G.F., 1996, Measurement of topography using polarimetric SAR data. *IEEE Transactions on Geoscience and Remote Sensing*, **34**, pp. 1266–1277.
- SCHULER, D.L., AINSWORTH, T.L., LEE, J.S. and DE GRANDI, G.F., 1998, Topography mapping using polarimetric SAR data. *International Journal of Remote Sensing*, **19**, pp. 141–160.
- SHI, J., WANG, J., HSU, A.Y., O'NEILL, P.E. and ENGMAN, T., 1997, Estimation of bare surface soil moisture and surface roughness parameter using L-band SAR image data. *IEEE Transactions on Geoscience and Remote Sensing*, **35**, pp. 1254–1265.
- SIMONETTO, E., 2002, Extraction 3D de structures industrielles sur des images Ramsès haute résolution par radargrammétrie. PhD thesis of the University Rennes 1, France.
- SMALL, D., 1998, Generation of digital elevation models through spaceborne SAR interferometry, *Remote Sensing Series*, vol. 30 (Switzerland: Remote Sensing Laboratories, Department of Geography, University of Zürich-Irchel).
- THOMAS, J., KOBER, W. and LEBERL, F., 1991, Multiple-image SAR shape from shading. *Photogrammetric Engineering and Remote Sensing*, **57**, pp. 51–59.
- TOUTIN, T., 1996, Opposite-side ERS-1 SAR stereo mapping over rolling topography. *IEEE Transactions on Geoscience and Remote Sensing*, **34**, pp. 543–549.
- TOUTIN, T., 2000, Evaluation of radargrammetric DEM from RADARSAT images in high relief areas. *IEEE Transactions on Geoscience and Remote Sensing*, **38**, pp. 782–789.
- TOUTIN, T. and GRAY, L., 2000, State-of-the-art of elevation extraction from satellite SAR data. *ISPRS Journal of Photogrammetry and Remote Sensing*, **55**, pp. 13–33.

- ULABY, F.T. and DOBSON, M.C., 1989, *Handbook of Radar Scattering Statistics for Terrain* (Dedham, Massachusetts: Artech House, Inc.).
- ULABY, F.T., MOORE, M.K. and FUNG, A.K., 1986, *Microwave Remote Sensing, Active and Passive*, vol. 3 (Norwood, Massachusetts: Artech House).
- WILDEY, R.L., 1986, Radarclinometry for the Venus radar mapper. *Photogrammetric Engineering and Remote Sensing*, **52**, pp. 41–50.
- WILSON, R.C. and HANCOCK, E.R., 1999, A reflectance model for radar shape from shading. *Proceedings of the 10th British Machine Vision Conference, Nottingham, UK, September 1999*, vol. 1, pp. 153–162.
- ZRIBI, M., TACONET, O., LE HÉGARAT-MASCLE, S., VIDAL-MADJAR, D., EMBLANCH, C., LOUMAGNE, C. and NORMAND, M., 1997, Backscattering behavior and simulation comparison over bare soils using SIRC/XSAR and ERASME 1994 data over Orgeval. *Remote Sensing of Environment*, **59**, pp. 256–266.
- ZRIBI, M., CIARLETTI, V. and TACONET, O., 2000, Validation of a rough surface model based on fractional brownian geometry with SIRC and ERASME radar data over Orgeval site. *Remote Sensing of Environment*, **73**, pp. 65–72.